Investigation of Turbulent Jet Impingement in a Confined Crossflow

G. D. Catalano,* K. S. Chang,† and J. A. Mathis†
Louisiana State University, Baton Rouge, Louisiana

Measurements and computations are reported for the flow of a turbulent jet discharging into a crossflow confined between two parallel plates. For jet-to-crossflow velocity ratios R equal to 2 and 4, mean and fluctuating velocity components are measured by laser-Doppler anemometry. Calculated results are obtained by solving the steady, three-dimensional elliptic forms of the Reynolds equations coupled with the two-equation $k-\varepsilon$ model of turbulence. Comparison of calculated results with experimental data shows good agreement in the downstream region but only fair agreement in the initial region. Results also show that impingement of the jet on the opposite wall occurs at a velocity ratio of $R = 4$.

Nomenclature

C	= species concentration
C_J	= species concentration at the jet entrance
c_1, c_2, c_μ	= constants in turbulence model
D	= jet diameter at the injection
d_f	= fringe spacing
d_{pv}	= probe-volume diameter
H	= channel spacing
k	= turbulent kinetic energy
l_{pv}	= probe-volume length
P	= effective pressure, $p + 2/3\ \rho k$
p	= pressure
R	= velocity ratio, V_J/U_0
U,V,W	= mean velocity components
u,v,w	= fluctuating velocity components
U_0	= cross stream velocity (tunnel flow speed)
V_J	= jet injection velocity
x,y,z	= Cartesian coordinates
y^+	= dimensionless value of $y(=\rho k^{1/2} c_\mu^{1/4} y/\mu)$
Γ_Φ	= diffusion coefficient
ε	= dissipation rate of k
θ	= beam-intersection angle
λ	= underrelaxation factor
λ_{laser}	= wavelength of laser beam
μ	= molecular viscosity
Φ	= general dependent variable
ρ	= density
$\sigma_T, \sigma_k, \sigma_\varepsilon$	= turbulent Prandtl/Schmidt numbers
Ω_x	= x-direction mean vorticity
$(\tilde{\ })$	= rms of quantity

Introduction

THE flowfield produced by a single jet discharging into a unbounded crossflow has been examined by many investigators including Crabb et al.,[1] who also provided an extensive review of earlier work. One important feature of the jet in a cross stream is the deflection of the jet trajectory and the creation of a bluff body wake in the cross stream. Another feature of the flowfield is the production of a pair of counter-rotating vortices created by the shear along the edges of the jet. If the velocity ratio is large enough to permit impingement on the opposite plate, additional complexities arise in the flowfield. The effect of the confining surface is examined in this work.

Turbulent jets in confined crossflows have received considerably less attention. Such configurations are relevant for many practical applications such as gas-turbine combustors, the internal cooling of turbine blades, and V/STOL aerodynamics. Stoy and Ben-Haim[2] reported measurements of jet trajectories for a single blockage ratio ($H/D = 3.05$) and provided empirical correlations of the impingement point in terms of the velocity ratios for $2.5 \le R \le 7.0$. Holdeman and Walker[3] investigated a geometry relevant to diffusion air jets in gas-turbine combustion chambers. Their measurements encompassed temperature fields for both a single jet and a row of jets in a confined crossflow. This data was then used to develop correlations characterizing the behavior of the jet in terms of flow and geometric variables. Kamotani and Greber[4] presented both velocity and temperature measurements of a single jet, a row of jets, and two opposing jets in a crossflow. The experiments were performed over a wide range of velocity ratios and geometric variables. So far, no documentation of turbulent quantities for the confined problem have been provided.

This paper presents both numerical calculations and experimental results for the mean and fluctuating velocity components and scalar fields of the confined problem for jet-to-crossflow velocity ratios R of 2 and 4 at a fixed spacing between two parallel plates ($H/D = 10$). The aim of this study is to provide reliable measurements of the turbulent flowfield for test cases of the present calculation procedure and, as a consequence, to increase our understanding and ability to predict this complex flow.

The mean and fluctuating velocities were recorded with a laser-Doppler anemometer (LDA) system adapted for the measurement of highly turbulent flows and recirculating flows. Such a system allows highly accurate, nonintrusive measurements. The calculation procedure employed a finite-difference scheme for the solution of the three-dimensional elliptic forms of the Reynolds equations. The Reynolds stresses appearing in the time-averaged equations are calculated by the two-equation model of turbulence in which the transport equations are solved for the turbulent kinetic energy k and its dissipation rate ε.

Received Nov. 7, 1988; revision received Jan. 16, 1989,

*Associate Professor, Mechanical Engineering, Member AIAA.
†Graduate Assistant, Mechanical Engineering.

Mathematical Model

Governing Equations

The flowfield under consideration is governed by the fully three-dimensional forms of the partial differential transport equations for mass, momentum, and species. Most current turbulence models rely on the solution of the Reynolds-averaged equations in which the dependent variables are decomposed into time-averaged and fluctuating components. The time-averaged equations are exact, since no assumptions have been introduced in their derivation. However, they cannot be solved, because the stress terms (usually called the Reynolds stresses) arising from the turbulent motion appear as additional unknowns. Accordingly, additional assumptions regarding the relationship between the Reynolds stresses and the time mean variables must be incorporated into the turbulence model. In the $k-\varepsilon$ model, the Reynolds stresses are related to the mean rate of strain via the Boussinesq eddy-viscosity concept. The turbulent or eddy viscosity is expressed in terms of the turbulent kinetic energy k and its dissipation rate ε. The standard version of the $k-\varepsilon$ model proposed by Launder and Spalding[5] is used for the calculation procedure. In Cartesian tensor notation, the governing equations may be written in the following general form:

$$\frac{\partial}{\partial x_j}(\rho U_j \Phi) = \frac{\partial}{\partial x_j}\left(\Gamma_\Phi \frac{\partial \Phi}{\partial x_j}\right) + S_\Phi \tag{1}$$

Equations for continuity, momentum, species concentration, turbulent kinetic energy, and dissipation rate of turbulent kinetic energy are presented in Table 1, in terms of a general dependent variable Φ, a diffusion coefficient Γ_Φ, and a source term S_Φ.

Table 1. Governing equations[a]

Φ	Γ_Φ	S_Φ
1	0	0
$U_i, i = 1,2,3$	μ_t	$-\partial P/\partial x_i + \partial/\partial x_j[(\mu_t(\partial U_j/\partial x_i)]$
C	μ_t/σ_t	0
k	μ_t/σ_k	$G - \rho\varepsilon$
ε	μ_t/σ_ε	$(\varepsilon/k)(c_1 G - c_2\rho\varepsilon)$

[a] $P = p + 2/3\,\rho k$; $G = \mu_t[(\partial U_i/\partial x_j) + (\partial U_j/\partial x_i)]\partial U_i/\partial x_j)$; and $\mu_t = c_\mu \rho k^2/\varepsilon$. $c_\mu = 0.09$, $\sigma_t = 0.9$, $c_1 = 1.44$; and $c_2 = 1.92$, $\sigma_k = 1.0$, $\sigma_\varepsilon = 1.3$.

Calculation Method

The flow geometry under consideration and the coordinate system used is shown in Fig. 1. The flow is symmetric about the $x-y$ plane ($z = 0$). Computational results are obtained using a revision of the SIMPLE algorithm.[6]

The computations were executed on an IBM 3090 computer at Louisiana State University. A typical calculation using $20 \times 15 \times 15$ nodes required approximately 250 iterations and 14 min of CPU time. Computer storage limitations in the three-dimensional calculation necessitate the use of a relatively coarse grid distribution. With the variations of the dependent variables between grid points in the convection-diffusion problems exhibiting an exponential behavior, a truncated Taylor series in an upwind or central-difference scheme fails to be an adequate representation except for fine grid size. The power-law scheme adapted in this work provides an acceptable representation of the exponential behavior and therefore minimizes false diffusion. Demuren[7] provides estimation methods of false diffusion in three-dimensional calculations. However, for the present work, with the computer storage available at this time, it is difficult to refine the finite-difference grid further. There are, however, indications that the results are grid dependent, as the contour shapes are repeatable with a coarser grid size ($15 \times 10 \times 10$) but the magnitude of, for example, the x component of mean velocity may vary up to 10%.

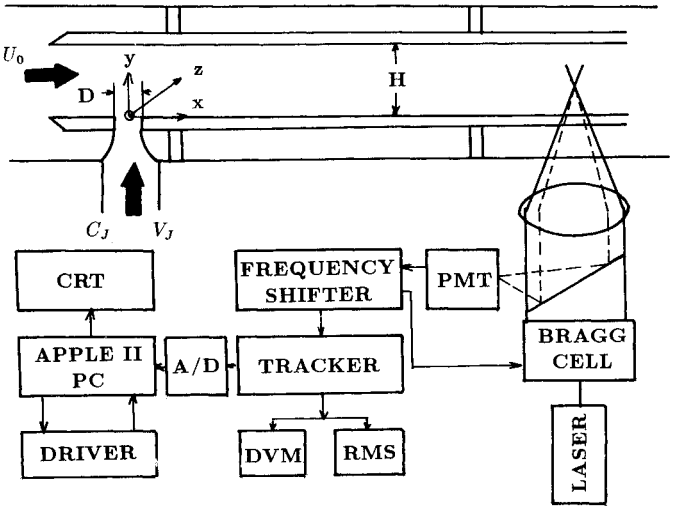

Fig. 1 Schematic diagram of experimental setup.

At each iteration, it is necessary to employ underrelaxation when solving the algebraic equations (i.e., $\Phi = \lambda\Phi_{new} + (1-\lambda)\Phi_{old}$). The number of iterations and the stability/divergence of the solutions are directly affected by the value of the underrelaxation factor λ. Typical values of λ used are $\lambda = 0.2$ to 0.4 for the velocity components and $\lambda = 0.5$ for all scalar variables. The iteration terminates when the normalized sum of the mass source, which is a representation of the error in the mass conservation equation, is less than 10^{-5} and the variations of all the dependent variables between two successive iterations are less than 0.1%.

Boundary Conditions

All of the dependent variables must be specified at the inflow boundary and the jet exit. The boundary conditions are prescribed, when possible, from the experimental measurements. This data includes the x-component velocity at the upstream boundary and the y-component velocity at the jet exit.

1) At the upstream boundary, $U = U_0$, $V = W = C = 0$, $k = 0.003U_0^2$, and $\varepsilon = k^{3/2}/0.06H$, where the turbulent field is assumed isotropic.

2) At the jet exit, $V = V_j$, $U = W = 0$, $C = 1.0$, $k = 0.002V_j^2$, and $\varepsilon = k^{3/2}/0.6D$, where $k = (v^2 + 2u^2)/2$, and assumes a homogeneous flow in the x and z directions.

At the downstream plane, the gradients of all of the dependent variables in the x direction are equal to zero. Practically, the location of the downstream edge was adjusted such that local variations of dependent variables are small, for example, less than 1% of those of the inlet stream. This fully developed condition was achieved at $x/D = 24$ for $R = 2$ and at $x/D = 32$ for $R = 4$. At the symmetric plane, the normal gradients of all of the dependent variables except the normal velocity component are taken to be zero; the normal velocity is taken to be zero ($W = 0$).

The location of the grid line nearest the wall is adjusted such that all of the grid points on the line occur in the fully turbulent region ($11 < y^+ < 300$) where the logarithmic wall law profiles are valid. A two-layer model of the wall-function method proposed by Chieng and Launder[8] is employed. In this method, the dependent variables are patched onto the wall law profiles and the mean generation rate and the dissipation rate in the kinetic energy equation are evaluated by accounting for the local variations of the turbulent quantities near the wall.

The half-circular nozzle in the bottom plate is presented in the Cartesian coordinate system by eight rectangular cells. The cell's surface areas are modified so that the specified jet velocity produces the correct mass fluxes through the surface.

Experimental Setup and Measurement System

The experiments are performed in a subsonic wind tunnel in the Experimental Fluid Dynamics Laboratory of the Mechanical Engineering Department at Louisiana State University. The dimensions of the test section are 60-cm wide, 45-cm high, and 180-cm long. The nearly uniform flow in the test section is attained by routing the airflow through a 12:1 contraction section and flow-straightening honeycomb tubes. The freestream turbulent intensity is less than 0.8% in the range of tunnel velocities (9.5–50.0 m/s). Optical access for the LDA measurements is provided through a removable plexiglass wall in the test section.

The jet stream is supplied from the laboratory's compressed air system and adjusted by a high-precision pressure regulator. In order to minimize the effect of the tunnel wall boundary layer, the jet exit is mounted flush onto a plate placed 12 cm above the bottom wall of the tunnel and the jet is aligned with the test section centerline. The maximum obtainable jet velocity is approximately 50.0 m/s and the corresponding Reynolds number based on the 1.27-cm jet diameter is 3.9×10^4.

The near-exit plane mean velocity profiles of the jet flowfield are presented in Fig. 2 for $R = 2$ and $R = 4$. The turbulent intensities $\tilde{v}/V_J$ are equal to 5.0% for the lower value of R and equal to 1.4% for the higher value. Although not described here, the autospectra of the jet exit field did not exhibit a potential core behavior for $R = 2$.

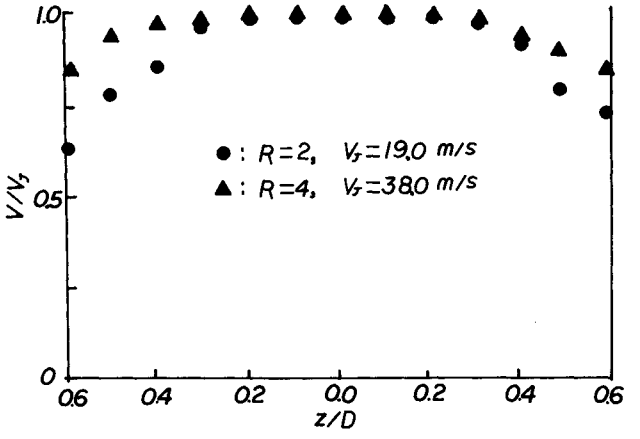

Fig. 2 Free jet mean velocity profiles at $y/D = 1.0$ and $x/D = 0.0$.

The velocity-ratio values are achieved by adjustment of the compressed-air-line pressure regulator on the jet flow system while keeping the tunnel flow fixed at 9.5 m/s. The assumption of symmetry of the entire flowfield about the plane $z = 0$ was also validated. In the work presented here, all of the experimental data was obtained in the plane of symmetry.

The details of the LDA setup are as follows:

Beam-intersection angle, $\theta = 7.25$ deg
Fringe spacing, $d_f = 5$ μm
Probe-volume diameter, $d_{pv} = 0.25$ mm
Probe-volume length, $l_{pv} = 3.6$ mm
He–Ne laser rated at 15 mW, $\lambda_{\text{laser}} = 632.8$ nm

The jet stream and the freestream are seeded with olive-oil particles using an aerosol generator. The mean oil-droplet diameter is estimated to range from 0.8–3.0 μm. This particle-diameter range is appropriate to follow airflows where turbulence frequencies exceed 1 kHz.[9]

The Doppler signal from the detector (Photomultiplier) is analyzed by a TSI LDA Tracker System Type 1090. Note that both the jet and the crossflow are marked, thus enabling the use of the tracker processor. The signals are first amplified to an optimum signal-to-noise ratio and passed through selectable bandpass filters prior to the signal analysis. The tracker, which is a phase-locked-loop (PLL) device, converts the Doppler signal into a continuous velocity signal as long as at least one particle is present in the probe volume at every time. At the low particle arrival rate, the continuous signal is attained by a sample-and-hold circuit of the tracker, which holds the previous reading until a new valid signal is retrieved. The resulting instantaneous velocity signal from the tracker is analyzed by an Apple IIe microcomputer after conversion from analog signal to digital signal. Direct current and rms voltmeters are used for the data validation. Mean and rms velocities are averaged using more than 10^3 data points with a data rate equal to 2 kHz. The data is also corrected for velocity bias. All of the experimental results are repeatable within 5%.

When measuring the vertical velocity component and the Reynolds stresses, the optical system is rotated $\pm$ 30 deg in the x–y plane. The Reynolds stresses are calculated by averaging the projections of the velocity fluctuations in the plane.

Results and Discussions

The jet-to-cross-stream velocity ratios (R) investigated were 2 and 4. The spacing between the parallel plates is fixed at 10 jet diameters and each side wall is located 15 jet diameters from the jet center. Figure 3 shows isocontour plots of the nondimensionalized species concentration C/C_J in the plane of symmetry. The contours indicate the extent of the penetration of the marked jet particles into the outer stream. With the presentation of the isocontours, the line S of maximum maximorum (i.e., maximum of maximums) is identified. From this line, a qualitative representation of the flowfield is achieved including the extent of the jet deflection and the existence of impingement. Note that impingement does not occur for $R = 2$. Total mean velocity vectors in the plane of symmetry of the flowfield are shown in Fig. 4. With $R = 4$, significant upward motion continues farther downstream. For the case of $R = 2$, the jet is deflected downward near the jet discharge and more rapidly aligned with the cross stream. Note the wake regions in the outer flow immediately upstream and downstream of the jet entrance.

The predicted isocontours of the scalar field at three trans-

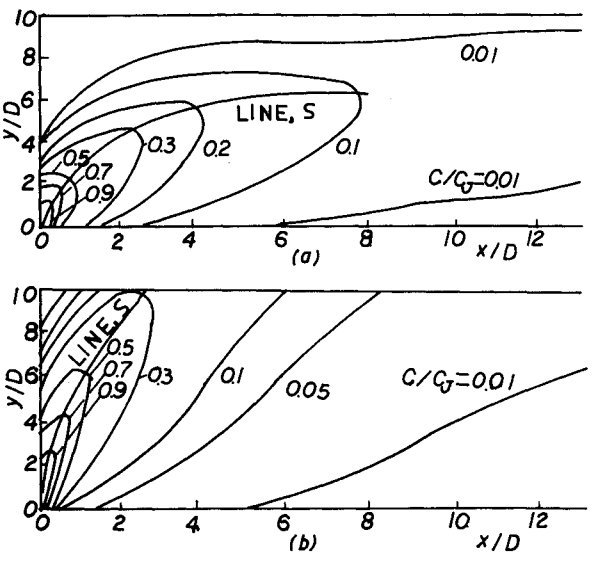

Fig. 3 Dimensionless scalar field C/C_J and line of maximum maximorum, S, in x–y plane ($z = 0$): a) $R = 2$; and b) $R = 4$.

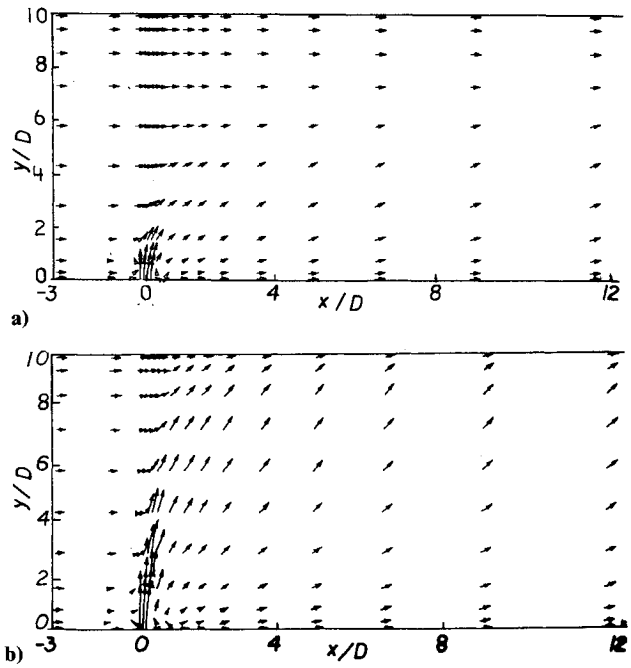

Fig. 4 Mean velocity vectors in $x-y$ plane: a) $R=2$; and b) $R=4$.

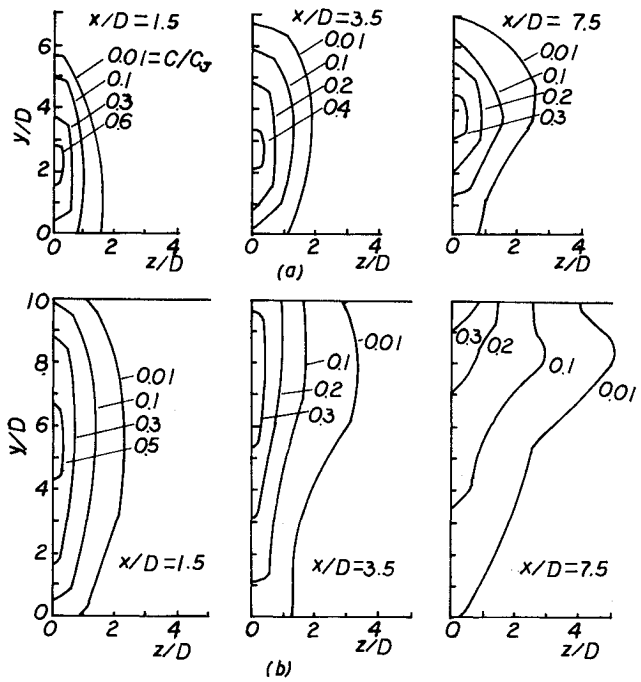

Fig. 5 Scalar field C/C_J in $y-z$ plane at several downstream locations: a) $R=2$; and b) $R=4$.

verse cross sections downstream are presented in Fig. 5 for both the velocity ratios of 2 and 4. The top wall is not shown for $R=2$ (Fig. 5a). The results indicate that the diffusion characteristics of the jet stream strongly depend on the velocity ratio. For the lower velocity ratio, the jet is deflected rapidly by the influence of the cross-stream momentum. The jet stream is convected downstream and diffuses out in both the vertical and transverse directions (y and z directions, respectively). In the case of the higher velocity ratio, the jet stream directly impinges on the opposite plate and diffuses more rapidly in the side direction (z direction). The kidney-shaped cross section of the jet is clearly seen as the jet develops downstream. The point of the maximum scalar value occurs on the top wall and along the centerline after the impingement.

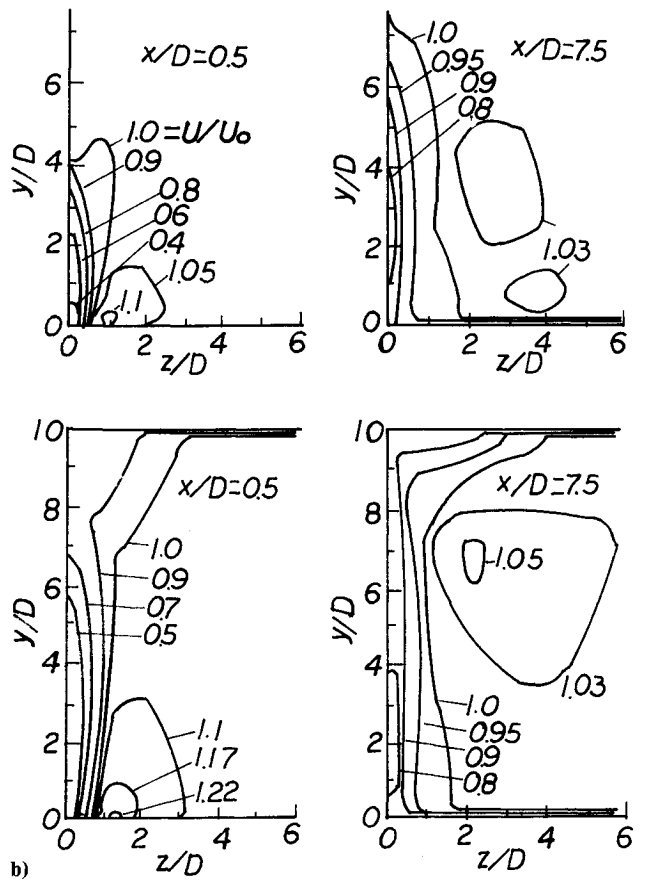

Fig. 6 Streamwise component of mean velocity contours, U/U_0 in $y-z$ plane: a) $R=2$; and b) $R=4$.

Figure 6 shows contours of the x-direction mean velocity in the $y-z$ planes at two downstream locations. The velocity is nondimensionalized with the cross-stream velocity. In the initial region, the crossflow is accelerated around the edge of the jet and produces a velocity maxima near side of the jet discharge. In Fig. 6, the jet stream gradually gains axial-direction momentum as it is convected downstream. Note that the cross stream is deflected sideways in the initial region. This cross stream then accelerates the jet stream from the edges of the jet cross section after the jet is aligned with the cross stream.

As mentioned previously, a major feature of a jet in a crossflow is the production of the counter-rotating vortices, which are created by the shear along the edge of the jet. Numerical calculations of this study predict the vortex production (Fig. 7). The streamwise component of mean vortices is calculated from the velocity vectors in the cross-section planes. Here, the vorticity is defined as follows:

$$\Omega_x = \frac{\partial(W/U_0)}{\partial(y/D)} - \frac{\partial(V/U_0)}{\partial(z/D)} \tag{2}$$

Only the vortices in the half-plane extending from the symmetric plane are presented. The opposite half-plane can be visualized with an opposite sign of the vortex strength. The core of the vortex structure in each plane is seen to propagate towards the upper surface as it is convected downstream. The cross-sectional shape of the vortex structure seems to be similar to that of the scalar field drawn in the same cross-section planes (see Fig. 5) except for the wake formed near the bottom wall. It is interesting to note that the vortex structure still exists after the jet impinges on the wall (Fig. 7b).

Two components of mean velocity are compared with experimental results at four downstream locations in the $x-y$ plane (Figs. 8 and 9). The results show that agreement is

generally fair. The main discrepancy, however, is the axial-direction velocity component U, especially in the upstream regions where the flow exhibits strong anisotropy. The streamwise component velocity profiles both at $R=2$ and $R=4$ clearly show wake behavior of the flow behind the jet and close to the wall. The wake region is induced by the backflow of the cross stream into the low-pressure region immediately downstream of the jet discharge. The wake region extends downstream but "lifts off" from the lower wall due to the strong inflow of the cross stream towards the symmetric plane. This inward motion carries high-momentum fluid from the cross stream to the symmetric plane. Therefore, the axial-component velocity profiles gradually smooth out downstream.

Measurements of the turbulent distributions are presented in Fig. 10 for $R=4$ at four downstream locations in the $x-y$ plane. The turbulent shear stress $\overline{uv}$ are compared with the calculation of the k-ε model. Again the agreement is less in

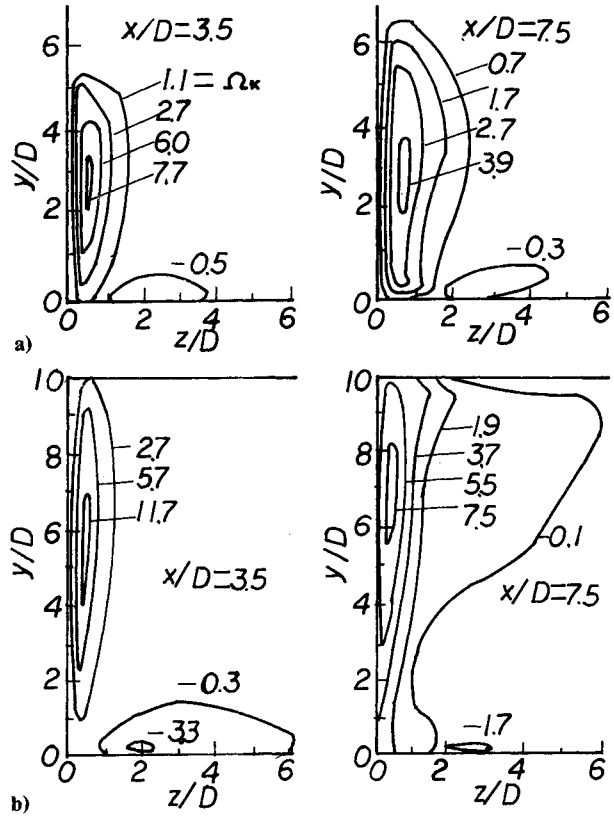

Fig. 7 Streamwise component of mean vorticity contours, $\Omega_c = |\partial(W/U_0)/\partial(y/D)| - |\partial(V/U_0)/\partial(z/D)|$: a) $R=2$; and b) $R=4$.

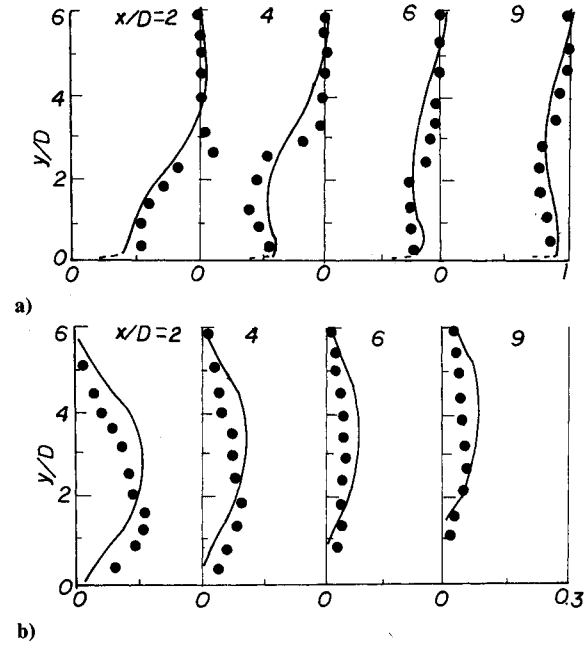

Fig. 8 Comparison between predicted profiles and experimental data in $x-y$ plane at $R=2$. ●, measurement and —, prediction: a) U/U_0; and b) V/V_J.

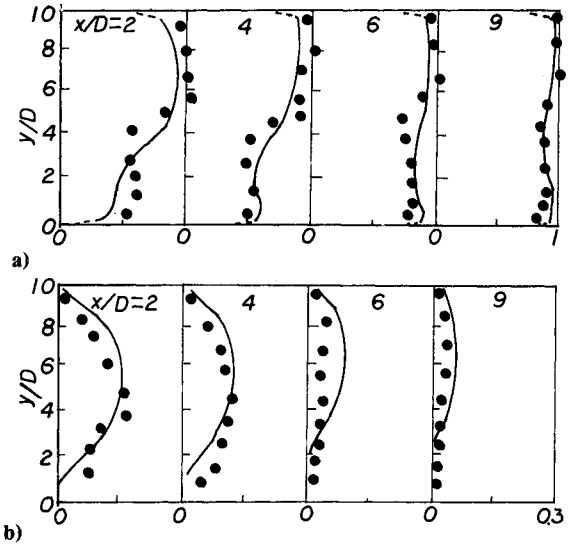

Fig. 9 Comparison between predicted profiles and experimental data in $x-y$ plane at $R=4$. ●, measurement and —, prediction: a) U/U_0; and b) V/V_J.

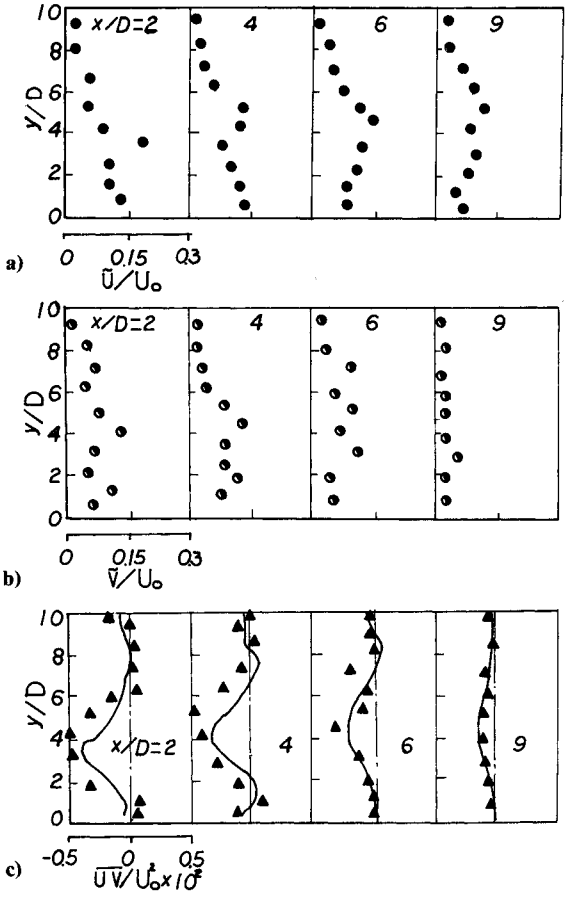

Fig. 10 Normalized Reynolds stress distributions in $x-y$ plane at $R=4$ a) $\tilde{u}/U_0$; b) $\tilde{v}/U_0$; and c) $\overline{uv}/U_0^2$, where ▲ is measurement and — is k-ε model.

the initial region. Moving downstream there is a tendency towards an isotropic flow and the agreement improves. The position of the maximum $\tilde{u}$ and $\overline{uv}$ profiles corresponds approximately to the center of the jet cross section where the velocity gradients $\partial U/\partial X$ and $\partial U/\partial Y$ are maximum. The $\tilde{v}$ profile maximum corresponds to the edges of the jet where $\partial V/\partial Y$ is maximum. Recalling from the turbulent and mean kinetic energy equation, the maximum transfer energy from the mean flow to the turbulent flow occurs when $|\overline{\rho u_i u_j}||\partial U_i/\partial X_j|$ is maximum. Thus, the turbulent intensities which are an indication of the level of turbulence will be a maximum when the Reynolds stresses and mean velocity gradient are maximum.

Summary

The present computational and experimental investigation demonstrates the validity of the following observations:

1) The jet trajectory and the existence of impingement are strongly dependent on the velocity ratio. For $R = 2$, no impingement occurs for a plate separation of ten jet diameters.

2) The cross stream is deflected laterally in the region near the jet entrance. The jet is deflected downward by the total pressure forces. The high shear around the jet edges in the near field results in a double vortex structure. The vortex structure extends far downstream.

3) A wake region exists immediately downstream of the jet discharge, but "lifts off" from the lower wall due to the strong inflow of the cross stream towards the symmetric plane.

4) The turbulence field is highly anisotropic in the initial region, although there is tendency towards isotropy further downstream.

5) The two-equation model of turbulence, with comparison to experimental data, predicts the flow downstream accurately but exhibits only fair agreement in the initial region where the flow is highly anisotropic.

Acknowledgments

This work was supported by the Flight Dynamics Laboratory, Air Force Wright Aeronautical Laboratories, Wright-Patterson AFB, Ohio, under Grant FY 1456-88-05065. The assistance of Dr. Joseph Shang and Dr. Phillip Webster, AFWAL/FIMM, is acknowledged.

References

[1]Crabb, D., Durão, D. F. G., and Whitelaw, J. H., "A Round Jet Normal to a Crossflow," *Transactions of ASME, Journal of Fluid Engineering*, Vol. 103, March 1981, pp. 142.

[2]Stoy, R. L. and Ben-Haim, Y., "Turbulent Jets in a Confined CrossFlow," Transactions of ASME, *Journal of Fluids Engineering*, Vol. 95, Dec. 1973, pp. 551.

[3]Holdeman, J. D. and Walker, R. E., "Mixing of a Row of Jets with a Confined Crossflow," *AIAA Journal*, Vol. 15, Feb. 1977, pp. 243.

[4]Kamotani, Y. and Greber, I., "Experiments on Confined Turbulent Jets in a Crossflow," NASA CR-2392, 1974.

[5]Launder, B. E. and Spalding, D. B., *Mathematical Models of Turbulence*, Chap. 5, Academic Press, London and New York, 1972.

[6]Patankar, S. V., *Numerical Heat Transfer and Fluid Flow*, Chap. 6, Hemisphere, Washington, DC, 1980.

[7]Demuren, A. O., "False Diffusion in Three-Dimensional Flow Calculations," *Computers and Fluids*, Vol. 13, 1985, pp. 411.

[8]Chieng, C. C. and Launder, B. E., "On the Calculation of Turbulent Heat Transport Downstream from an Abrupt Pipe Expansion," *Numerical Heat Transfer*, Vol. 3, 1980, pp. 189.

[9]Durst, F., Melling, A., and Whitelaw, J. H., *Principles and Practice of Laser Anemometry*, Chap. 10, 2nd ed., Academic Press, New York, 1981.